AGU PUBLICATIONS

Radio Science

RESEARCH ARTICLE

10.1002/2014RS005625

Digital signal processing for ionospheric propagation diagnostics

Charles L. Rino[1], Keith M. Groves[1], Charles S. Carrano[1], Jacob H. Gunter[2], and Richard T. Parris[3]

[1]Institute for Scientific Research, Boston College, Boston, Massachusetts, USA, [2]Department of Electrical and Computer Engineering, Utah State University, Logan, Utah, USA, [3]Air Force Research Laboratory, Ionospheric Hazards Specification and Forecast, Kirtland AFB, Albuquerque, New Mexico, USA

Key Points:
- Digital signal processing facilitates improved low-SNR performance
- Frequency tracking is required to extract narrowband modulation
- Simulation results establish performance bounds for TEC and scintillation diagnostics

Correspondence to:
C. L. Rino,
crino@comcast.net

Citation:
Rino, C. L., K. M. Groves, C. S. Carrano, J. H. Gunter, and R. T. Parris (2015), Digital signal processing for ionospheric propagation diagnostics, *Radio Sci.*, *50*, 837–851, doi:10.1002/2014RS005625.

Received 21 NOV 2014
Accepted 4 AUG 2015
Accepted article online 6 AUG 2015
Published online 31 AUG 2015

Abstract For decades, analog beacon satellite receivers have generated multifrequency narrowband complex data streams that could be processed directly to extract total electron content (TEC) and scintillation diagnostics. With the advent of software-defined radio, modern digital receivers generate baseband complex data streams that require intermediate processing to extract the narrowband modulation imparted to the signal by ionospheric structure. This paper develops and demonstrates a processing algorithm for digital beacon satellite data that will extract TEC and scintillation components. For algorithm evaluation, a simulator was developed to generate noise-limited multifrequency complex digital signal realizations with representative orbital dynamics and propagation disturbances. A frequency-tracking procedure is used to capture the slowly changing frequency component. Dynamic demodulation against the low-frequency estimate captures the scintillation. The low-frequency reference can be used directly for dual-frequency TEC estimation.

1. Introduction

Beacon satellite radio transmissions have been used for ionospheric diagnostics since Sputnik I was launched in 1957. The varying Doppler shift imposed by the changing range to the satellite was used initially to determine Sputnik's orbit. Later, Doppler tracking was used for position estimation with TEC corrections derived from dual-frequency measurements. Intensity scintillation caused by small-scale structure in the ionosphere was known from radio astronomy observations. Early research is summarized in the review article by *Swenson* [1994].

Technology evolved rapidly, but analog receivers were used for ionospheric diagnostics until fairly recently. Receivers developed for the wideband satellite beacon launched in 1975 processed simultaneous L band, UHF, and VHF signals, which were demodulated against an S band reference [*Fremouw et al.*, 1978]. Currently, satellites with Coherent Electromagnetic Radio Tomography (CERTO) beacons transmit L band, UHF, and VHF signals for ionospheric diagnostics [*Bernhardt and Siefring*, 2008]. With the advent of software-defined radio, analog receivers are being replaced with digital receivers that provide critically sampled baseband complex signals.

Digital processors for radio signals from satellite-borne transmitters must track the varying Doppler shift induced by changing path delay. This is true for Global Navigation Satellite System and narrowband beacon transmissions of interest here. The time-honored solution to efficient Doppler tracking is provided by phase-locked loops (PLLs). However, it is noteworthy that digital phase-locked loops operate with memory equal to the order of the loop transfer function. For example, the widely used second-order loop uses only two-signal samples to generate a phase correction update. The PLL efficiency is essential for real-time processing, but it requires a high signal-to-noise ratio (SNR). It is intuitively clear and borne out by analyses cited later in the paper that frequency estimates based on larger data blocks can achieve better low-SNR performance, albeit with significantly more computation.

The current generation of satellites that carry CERTO beacons do not support transmit antennas with uniform frequency-independent illumination; moreover, typical ground-mounted, broad-beam receiving antennas provide very little multipath or interference rejection. Consequently, digital or analog receivers that use conventional PLLs may not perform well. However, digital receivers operate at data rates (25 to 50 kHz) that allow horizon-to-horizon recording for post-pass processing. This provides an opportunity to exploit the improved performance that direct frequency tracking affords.

Yamamoto [2008] demonstrated a software-defined multifrequency receiver with a post-pass processing. The processing scheme, as described in section 4 of his paper, estimates a local spectral peak followed by narrow-band filtering and phase extraction. Figure 3 in his paper shows the extracted peak intensity and the frequency estimate derived from the processor. The signal intensities show uncorrelated variations over more than 20 dB, which is most likely multipath. Figure 4 in Yamamoto's paper shows a comparison of TEC estimates derived from a conventional receiver using phase tracking and his Fourier-domain method. The conventional receiver lost about 30% of the data, which can be attributed to loss of PLL lock under low-noise conditions.

This paper presents a detailed analysis of the performance that can be achieved with Fourier-domain processing schemes. We first review digital signal processing objectives. We then demonstrate a frequency-domain processing algorithm with simulated multifrequency noise-limited signals. Noise-limited signal realizations are generated by combining a slab TEC variation with simulated propagation disturbances. To the extent that the frequency-tracking scheme achieves the best performance commensurate with processing intervals that support linear frequency change, the simulation results establish performance bounds for TEC estimation and propagation diagnostics under strong scatter conditions.

The essential characteristics of a complex signal at the output of a beacon receiver low-noise amplifier are captured by the signal model

$$v(t) = \sqrt{\mathrm{SNR}(t)}\delta h(t; f_C)m\left(t + r(t)/c - K\overline{N}(t)/\left(2\pi f_C^2\right)\right)\exp\left\{2\pi i f_C\left(t + r(t)/c - K\overline{N}(t)/\left(2\pi f_C^2\right)\right)\right\} + e(t). \quad (1)$$

The deterministic signal amplitude component, $\sqrt{\mathrm{SNR}(t)}$, is defined by the signal-to-noise ratio (SNR)

$$\mathrm{SNR}\,(t) = \mathrm{SNR_m}/\left(r\,(t)\,/r_o\right)^2, \quad (2)$$

where $\mathrm{SNR_m}$ is the minimum SNR at the acquisition range r_o. The noise contribution, $e(t)$, has unity variance and is uncorrelated at the $\Delta t = 1/BW$ sample intervals. The parameter f_C is the center frequency, which is the formal phase reference. The parameter c is the vacuum velocity of light, $m(t)$ is an imposed complex modulation with unit average intensity and frequency range $-BW/2 < f < BW/2$. For efficient transmission $f_C >> BW/2$. The remaining model components, $K\overline{N}\,(t)\,/2\pi f_C^2$ and $\delta h_k(t; f_C)$, respectively, represent quasi-deterministic phase and complex stochastic modulations imposed by propagation through the ionosphere. A detailed development of (1) can be found in chapter 5 of *Rino* [2011].

Analog receivers remove the carrier term, $\exp\{2\pi i f_C t\}$, with mixing and filtering operations. Digital receivers sample the RF output directly, which amounts to replacing t in (1) by $t_0 + k\Delta t$. From the periodicity of the complex exponential, it follows that

$$\exp\left\{2\pi i\left(f_C\Delta tk\right)\right\} = \exp\left\{2\pi i\left(f_C\Delta tk - M\right)\right\}, \quad (3)$$

where M is an integer. If the digital sampling is locked to the carrier frequency, then $fc\Delta t$ is an integer as well, whereby the carrier term is unity. Formally, the under sampled radio-frequency signal has been aliased to baseband. The sampled complex data stream at the output of a digital receiver takes the simpler form

$$v_k = \sqrt{\mathrm{SNR}_k}\delta h(k\Delta t; f_C)m_k\exp\left\{2\pi i f_C\left(r_k/c - K\overline{N}_k/2\pi f_C^2\right)\right\} + e_k. \quad (4)$$

A smoothly varying background ionosphere induces a phase shift proportional to the integrated electron density variation along the propagation path:

$$\delta\phi = -r_e c/f\int\delta N_e \mathrm{d}l \quad (5)$$

$$= -(r_e c/f)\overline{N}, \quad (6)$$

where δN_e is the electron density variation, r_e is the classical electron radius, and

$$\overline{N} = \int\delta N_e \mathrm{d}l \ \ \text{electrons/m}^2 \quad (7)$$

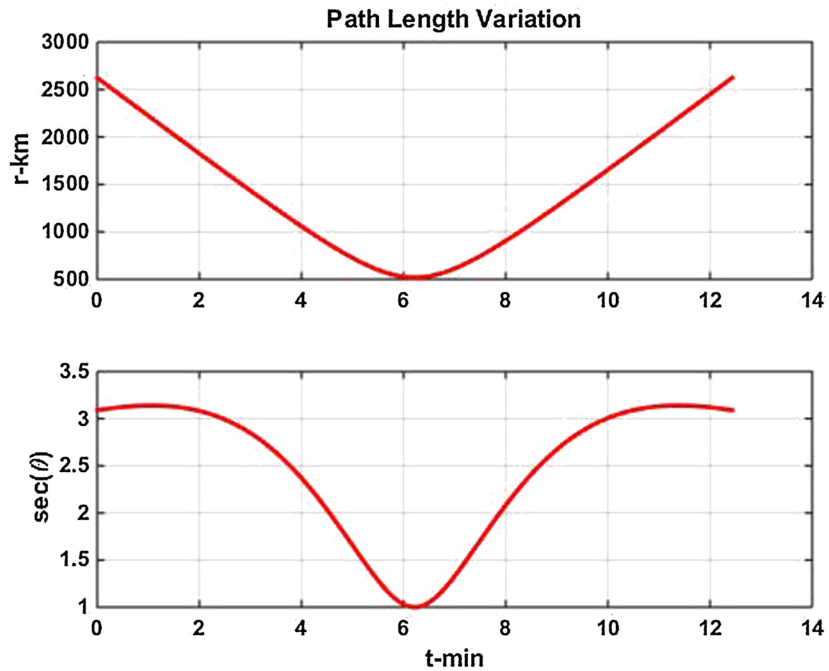

Figure 1. Circular overhead orbit range and slant path variation ($\sec(\theta_p)$) for T_p = 100 min, H_s = 1000 km, and H_P = 350 km.

represents the path-integrated electron density, which is measured in TEC units of 10^{16} electrons per square meter of integrated path length. The translation constants are conveniently absorbed in the K parameter

$$K = \frac{r_e c}{2\pi} \times 10^{16} = 1.3454 \times 10^9 \text{ m}^2/\text{s}. \tag{8}$$

The refractive index includes the constant background that establishes the propagation velocity in a uniform medium.

2. Simulated Digital Signals

Generating realizations of the signal defined by (4) requires construction of the stochastic transfer function, $\delta h(k\Delta t; f_C)$. The computation is greatly simplified by replacing the extended ionosphere by a one-dimensional

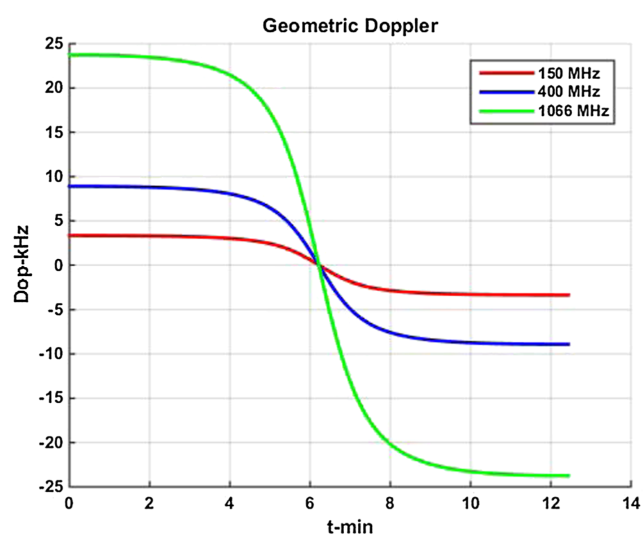

Figure 2. Doppler shifts induced by circular overhead orbit range change at CERTO beacon frequencies.

path integral, which we refer to as an equivalent phase screen. Moreover, *Carrano et al.* [2012] have shown that equivalent phase screens derived from two-dimensional projections onto the propagation plane are very effective for interpreting scintillation from predominantly cross-field paths. The projected two-dimensional geometry can be derived from orbital elements and the receiver location. However, for simulations, representative dynamics are captured by spherical Earth circular overhead orbits, which also facilitate slab TEC computation. An overhead circular orbit geometry is defined by the orbital period, T_p, the satellite height above the Earth, H_s, and the reference ionospheric penetration height, H_p. The vertical TEC, STEC0, and the SNR at the maximum visible range, $\mathrm{SNR_m}$, complete the signal specification. The orbit model formulae are summarized in the Appendix.

The upper frame of Figure 1 shows the horizon-to-horizon range variation for the representative low Earth orbit parameters $T_p = 100$ min, $H_s = 1000$ km, and $H_p = 350$ km. The lower frame is the secant of the propagation angle, which determines the path-length variation within a slab centered at H_p. The geometric Doppler shifts for the nominal CERTO beacon frequencies (150, 400, and 1066 2/3 MHz) are shown in Figure 2. The corresponding Doppler shifts induced by the TEC change with STEC0 = 50 TEC units are shown in Figure 3. The SNR variation induced by the range change (path loss) is shown in Figure 4 for $\mathrm{SNR_m} = 1$.

Ideally, forward propagation computations would be performed over local parallelogram segments as shown schematically in Figure 5. The magenta circular ionospheric intercept arc is approximated by 105 linear segments. An equivalent phase screen is centered on each segment. The directionally dependent complex field centered on the receiver is computed. With space-to-time conversion using the orbital velocity at the penetration point, the field can be interpreted as a time series segment. The field realization is constructed by concatenating the time series segments. A linear detrend forces the phase to be zero at the start and end of each segment, effectively removing the discrete phase change associated with the step direction change.

Stochastic structure is constructed by generating phase-screen realizations with two-component power law spectral density functions of the form

$$\Phi_{\delta\phi}(q) = C_p \varphi(q), \tag{9}$$

where $q = 2\pi/s$ is the magnitude of the spatial wave number,

$$\varphi(q) = \begin{cases} q^{-p_1} & q < q_0 \\ q_0^{p_2-p_1} q^{-p_2} & q > q_0 \end{cases}, \tag{10}$$

q_0 is the spatial wave number at which the power law index transitions from p_1 to p_2, and

$$C_p = r_e^2 \lambda^2 l_p C_s. \tag{11}$$

The parameters p_1, q_0, and p_2 are taken from published in situ measurements [*Basu et al.*, 1983]. For algorithm evaluation, it is convenient to impose the same turbulence level, C_p, for each slab. Although physically unrealistic, the varying propagation geometry generates a broad range of scintillation levels. The complete signal realization combines the deterministic components and the stochastic modulation. The stochastic contribution is interpolated to the 50 kHz rate required to capture the largest geometric Doppler shift at L band (see Figure 2).

The signal frequency content over time intervals long enough to resolve tens of Hertz is dominated by the geometric Doppler. Spectrograms constructed from sequential power spectral density functions (PSDs) are often used to display this *slow time* signal structure. The unwindowed PSD

$$P_n = \frac{1}{N} \left|\hat{v}_n\right|^2, \tag{12}$$

where $\hat{v}_n$ is the discrete Fourier transform (DFT)

$$\hat{v}_n = \sum_{k=0}^{N-1} v_k \exp\left\{-2\pi i n k/N\right\}, \tag{13}$$

resolves the discrete frequencies

$$f_{pn} = [0 : N/2-1, -N/2+1 : -1]\Delta f, \tag{14}$$

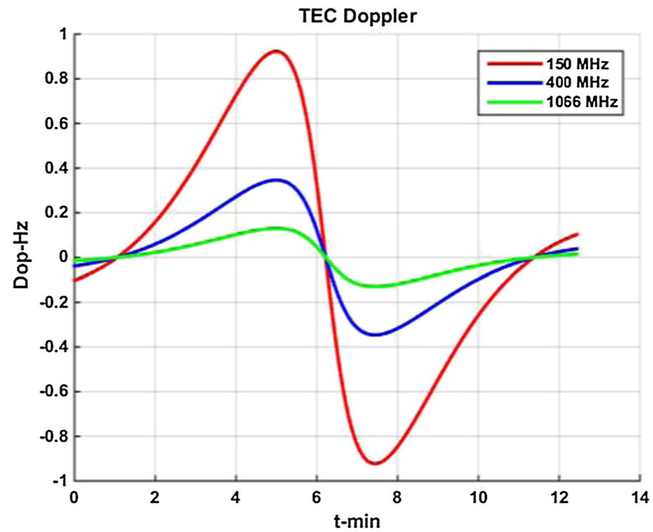

Figure 3. Doppler shifts induced by TEC change.

where $\Delta f = 1/(N\Delta t)$. Selection of the PSD interval $T = N\Delta t$ determines both the spectrogram frequency resolution $\Delta f = 1/T$ and the time for frequency change.

Typical signals as represented by (4) are confined to a few hundred Hertz about the mean Doppler shift. To the extent that the changing range to the satellite is known, the geometric Doppler can be removed by the dynamic demodulation operation

$$\overline{v}_k = v_k \exp\{-2\pi i f_C \overline{r}_k / c\}, \tag{15}$$

where r_k is the range to the k*th* segment reference. The demodulated signal can be filtered and downsampled to a frequency range that captures the modulation about the slowly changing geometric Doppler.

Figure 6 shows the SNR

$$\overline{\mathrm{SNR}}_k = |\overline{v}_k|^2 \tag{16}$$

obtained by dynamically demodulating a signal realization with the known geometric Doppler and downsampling with filtering to 500 Hz. The peak SNR in the absence of scintillation is 15 dB. At onset, the SNR is at

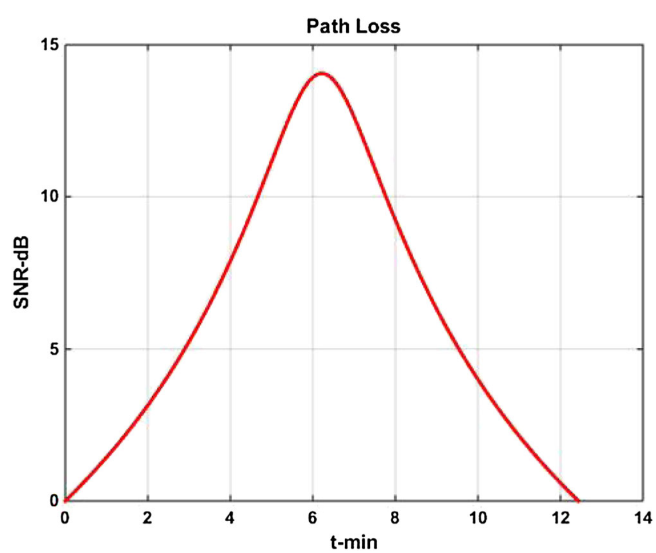

Figure 4. SNR variation induced by range change.

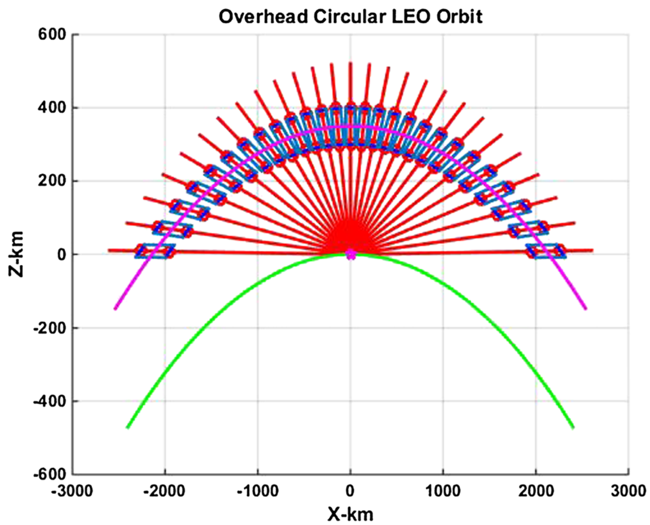

Figure 5. Schematic representation of disturbed regions about rays from source to receiver. Magenta curve is ionosphere penetration point.

the noise level (0 dB). Scintillation-induced fades drive the signal intensity to −40 dB. Fresnel filtering strongly suppresses contributions from the large-scale ionospheric phase structure that initiated the computation at the phase screen.

The demodulated signal phase,

$$\overline{\varphi}_k = \text{unwrap}\left(\arctan\left(Re\left(\overline{v}_k\right), Im\left(\overline{v}_k\right)\right)\right), \tag{17}$$

is more complicated. Large-scale phase structure dominates the signal phase even in the absence of the geometric Doppler contribution. Figure 7 shows the demodulated and downsampled signal phase after removal of the imposed TEC contribution. For algorithm evaluation, Figures 6 and 7 serve as scintillation truth.

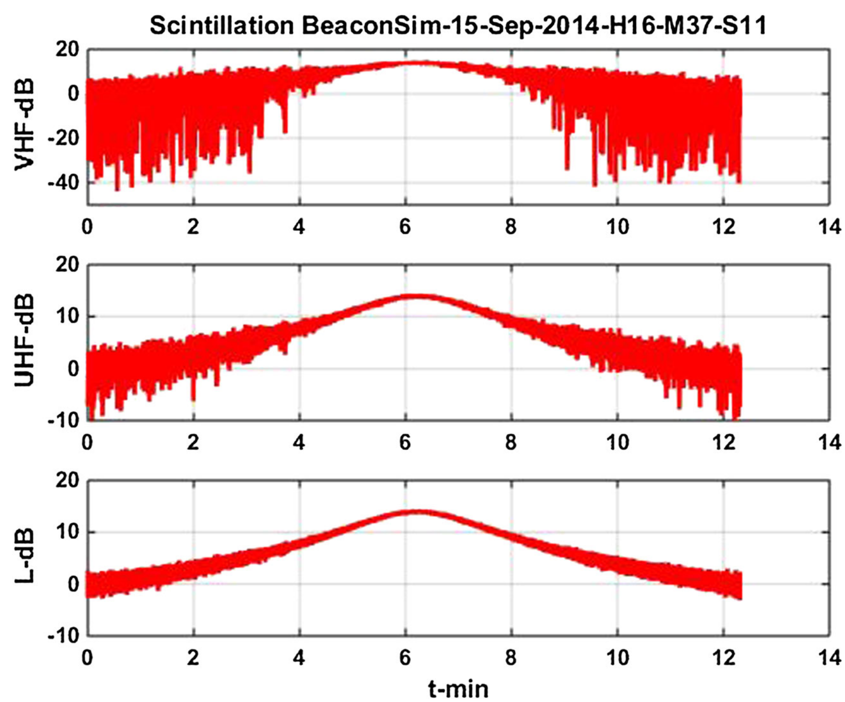

Figure 6. SNR variation of complex signal realizations with geometric Doppler removed following by filtered downsampling to 500 Hz.

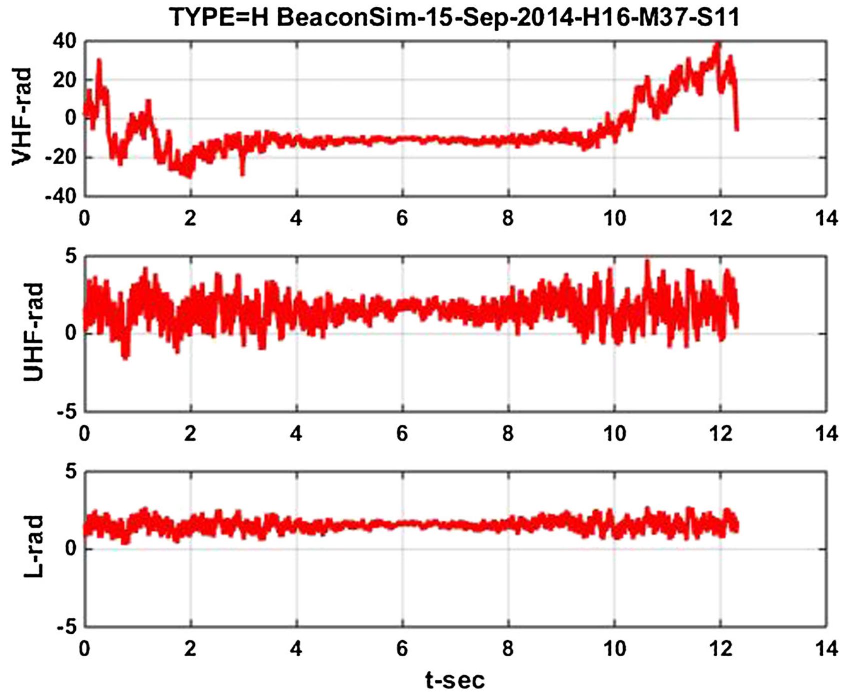

Figure 7. Scintillation phase derived from complex signal realization with geometric Doppler and imposed TEC removed.

The remainder of this paper describes and demonstrates a processing algorithm that first estimates the slow-Doppler variation of the signal. The slow-Doppler variation includes both geometric and TEC-induced components. Thus, the slow-Doppler estimate can be used directly for dual-frequency TEC estimation. Dynamic demodulation of the complex signal against the slow-Doppler estimate extracts the scintillation component.

3. Digital Signal Processing

Frequency tracking is the first signal processing operation for both narrowband and modulated signals. In effect, the estimated instantaneous frequency becomes the phase reference for all ensuing signal processing operations. If the transmitted signal is modulated, frequency tracking must be combined with waveform compression. Here only narrowband processing will be considered.

Analog receivers use phase-locked loops to track the signal frequency. The phase change associated with the slow-frequency variation is used to dynamically demodulate harmonically related signals. Let

$$\overline{\varphi}_k^{(n_r)} = 2\pi i f_C^{(n_r)} r_k/c - K\overline{N}_k/f_C^{(n_r)} + \phi_k + \epsilon \tag{18}$$

represent the reference oscillator phase for frequency reference index n_r. The phase of a lower frequency signals (indexed n) dynamically demodulated with the reference signal is

$$\varphi_k^{(n)} - \overline{\varphi}_k^{(n_r)}\left(f_C^{(n)}/f_C^{(n_r)}\right) = -K\overline{N}_k/f_C^{(n)}\left(1-\left(f_C^{(n)}/f_C^{(n_r)}\right)^2\right) + \phi^{(n)} - \overline{\phi}_k^{(n_r)}\left(f_C^{(n)}/f_C^{(n_r)}\right) + \epsilon \simeq -K\overline{N}_k/f_C^{(n)} + \phi^{(n)} + \epsilon. \tag{19}$$

Here the error term ϵ represents the background noise contribution. The approximation assumes that the frequencies are sufficiently well separated that reference-frequency propagation disturbances are negligible, which was the case for wideband. More often both frequencies admit propagation disturbances. In that case, phase estimates are combined to estimate TEC

$$\frac{1}{K}\frac{\overline{\varphi}^{(2)}/f_C^{(2)} - \overline{\varphi}^{(1)}/f_C^{(1)}}{1/\left(f_C^{(1)}\right)^2 - 1/\left(f_C^{(2)}\right)^2} = N_{\text{TEC}} - \frac{\overline{\phi}_k^{(2)}/f_C^{(2)} - \overline{\phi}^{(2)}/f_C^{(1)}}{1/\left(f_C^{(1)}\right)^2 - 1/\left(f_C^{(2)}\right)^2} + \epsilon. \tag{20}$$

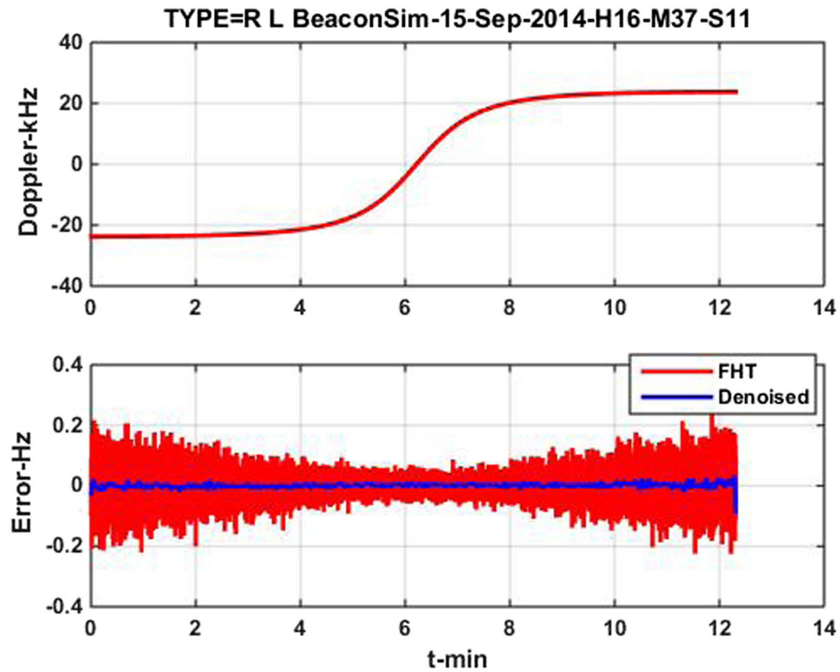

Figure 8. (top) VHF Doppler from R realization. (bottom) Error with no denoising (red) and denoising (blue).

3.1. Frequency Hypothesis Tracking

The time-varying frequency concept can be formalized by defining instantaneous frequency as

$$\delta f(t) = \frac{1}{2\pi}\frac{\mathrm{d}\varphi(t)}{\mathrm{d}t}. \tag{21}$$

The survey paper by *Boashash* [1992a] presents a detailed development. A companion paper by *Boashash* [1992b] reviews digital processing methods that can estimate instantaneous frequency. Section F of *Boashash* [1992b] describes a Fourier peak tracking method, which is identical to the frequency hypothesis tracking (FHT) method described in chapter 5 of *Rino* [2011]. A sub-bin frequency-tracking method described in chapters 7.14 and 10.11 of *Tsui* [2005] uses the same principle.

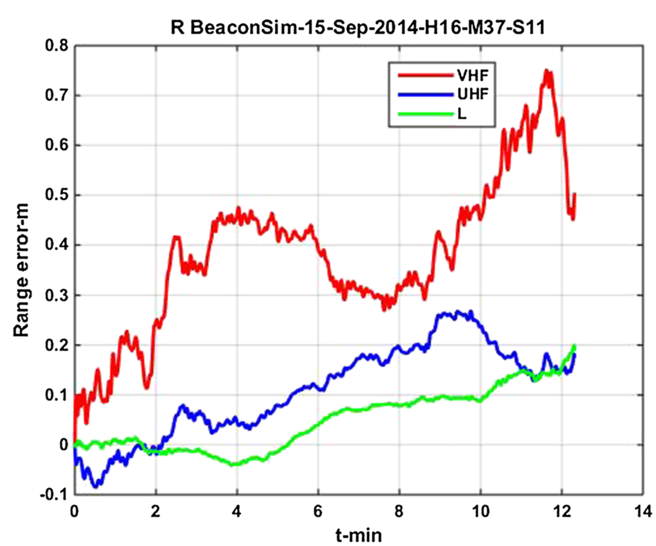

Figure 9. Range errors from estimates derived from R realization phase.

The concept underlying all these methods can be demonstrated by replacing nk/N in (13) with $k\Delta tn\alpha$, where α takes any value between the Nyquist frequency limits $\pm 1/(2\Delta t)$:

$$h(\alpha\Delta t) = \sum_{k=0}^{N-1} v_k \exp\{-2\pi ik\Delta t\alpha\}. \tag{22}$$

Fractional frequency is defined as the variation between the discrete DFT frequencies. That is,

$$\alpha/\Delta f = n + \delta, \tag{23}$$

where δ is a fraction between $-1/2$ and $1/2$. The fractional-frequency PSD is defined as

$$H(\delta) = |h(\alpha\Delta t)|^2 / N. \tag{24}$$

Assume that over the time interval T,

$$v_k \simeq \sqrt{\mathrm{SNR}} \exp\left\{2\pi\overline{\delta f}k\Delta t\right\} + e_k. \tag{25}$$

With (25) substituted for v_k, the expectation value of the fractional-frequency PSD becomes

$$\langle H(\delta)\rangle = \frac{\mathrm{SNR}}{N}\left|\sum_{k=0}^{N-1}\exp\left\{-2\pi ik(\delta - \overline{\delta f}/\Delta f)/N\right\}\right|^2 + 1 \tag{26}$$

$$= \mathrm{SNR}\frac{\sin^2\left(2\pi N\Delta t(\delta - \overline{\delta f}/\Delta f)\right)}{N\sin^2\left(2\pi\Delta t(\delta - \overline{\delta f}/\Delta f)\right)} + 1. \tag{27}$$

The maximum value,

$$\max\langle H(\delta)\rangle = N * \mathrm{SNR} + 1, \tag{28}$$

is achieved when $\delta = \overline{\delta f}/\Delta f$. The factor N represents a coherent processing gain that can be exploited.

To track a slowly changing frequency, $\max H(\delta)$ is computed for each block of N data samples offset by O samples. The samples within each block are defined by the sequences

$$k(m) = mN(1 - O/N) + k \; for 0 \le k \le N-1, m = 0, 1, \cdots, n\mathrm{blocks}. \tag{29}$$

The search is initiated with the peak frequency from the previous segment. A peak signal intensity estimate is recovered by evaluating $H(\delta)$ at the peak fractional frequency. Phase is recovered by trapezoidal-rule integration

$$\phi_{k+1} = \phi_k - 2\pi\left(f\mathrm{Dop}_k + f\mathrm{Dop}_{k+1}\right)T/2. \tag{30}$$

Offset and block size parameters are set to keep the phase change over the integration interval less than π radians. If this condition is not met, then the frequency estimation errors oscillate about the true frequency much like an out-of-lock phase tracking loop. Offsets less than $N/2$ do not reproduce the smallest-scale structure reliably.

To evaluate FHT, signal realizations were constructed at the Communication/Navigation Outage Forecast System CERTO beacon VHF, UHF, and L band frequencies. Realizations at each frequency were constructed with noise plus geometric range only (designated R), with noise plus geometric range and TEC only (designated T), and with noise plus geometric range, TEC, and scintillation (designated H). FHT tracking with $N = 4096$ and $O = 2048$ was performed for each realization. The FHT output reports at intervals

$$T_{\mathrm{seg}} = Odt = 41 \text{ ms } (24.41 \text{ Hz}) \tag{31}$$

include SNR, fDop, phase, and a lock flag indicating that the FHT SNR was greater than a set threshold of 15 dB.

Figure 8 (top) shows the VHF Doppler from the R realization. The red curve in Figure 8 (bottom) is the difference between the true geometric Doppler and the FHT estimate. The uncorrelated Doppler errors vary with SNR.

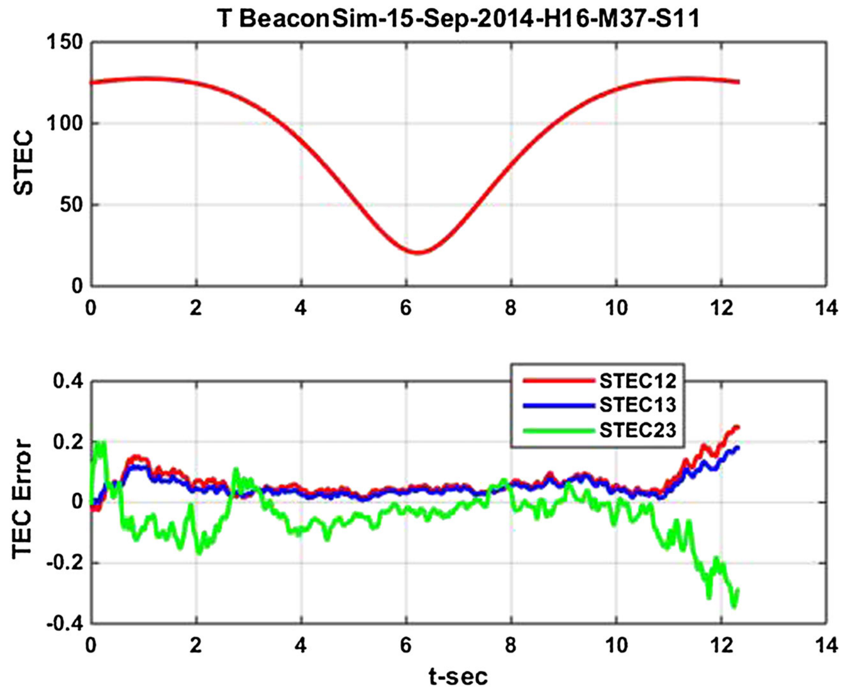

Figure 10. (top) TEC and errors using T realizations.

Wavelet-based denoising as described in chapter 11.3 of *Mallat* [2005] was applied to the FHT Doppler. Phase derived from denoised Doppler estimates is defined by (30). To present the phase errors in physical units, Figure 9 shows the range errors incurred by replacing ϕ_k in the relation

$$\hat{r}_k = c\phi_k / \left(2\pi f_C\right) \tag{32}$$

with the R realization phase. The range errors are less than 1 m, but they exhibit trend-like variations attributed to the integral relation between phase and frequency. Integrating uncorrelated noise samples produces Brownian motion, which has a $1/f$ Fourier spectrum leading to the trend-like departures from strict stationarity. Power law phase noise is a well-known characteristics of oscillators [*Lee and Hajimiri*, 2000].

Dual-frequency denoised FHT Doppler estimates can be used directly to estimate TEC by substituting phase pairs into (20). The Doppler errors for the T realizations are indistinguishable from the errors shown in Figure 8.

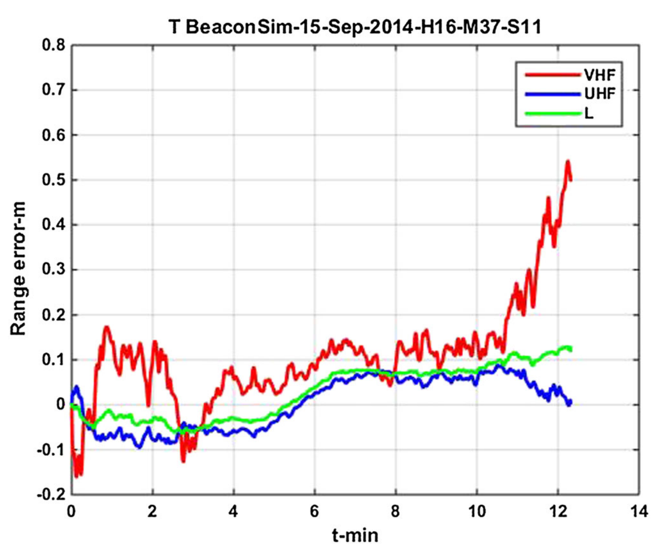

Figure 11. Corrected range estimates from (33) using phase estimates and dual-frequency T realizations.

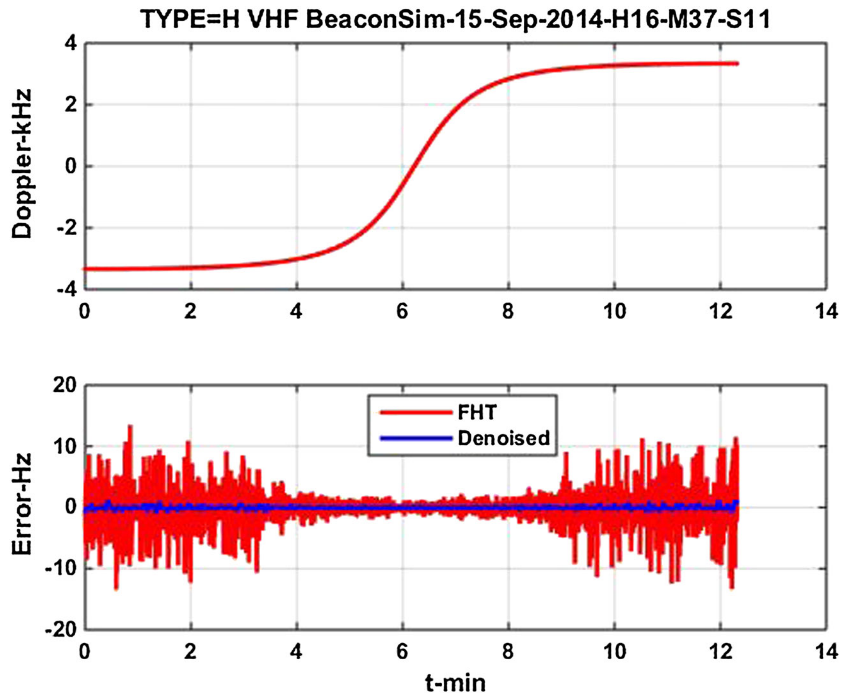

Figure 12. (top) VHF Doppler from H realization. (bottom) Error with no denoising (red) and denoising (blue).

The upper frame of Figure 10 shows the TEC truth offset to generate a physical TEC variation. The lower frame summarizes T-realization TEC errors obtained from three C/NOFS frequency pairs. The numbers 1,2,3 refer to VHF, UHF, L band, respectively. The noise-limited errors are significantly less than 1 TEC unit. Although phase meander can be ascertained in the errors, it appear to be mitigated by the difference operation in (20).

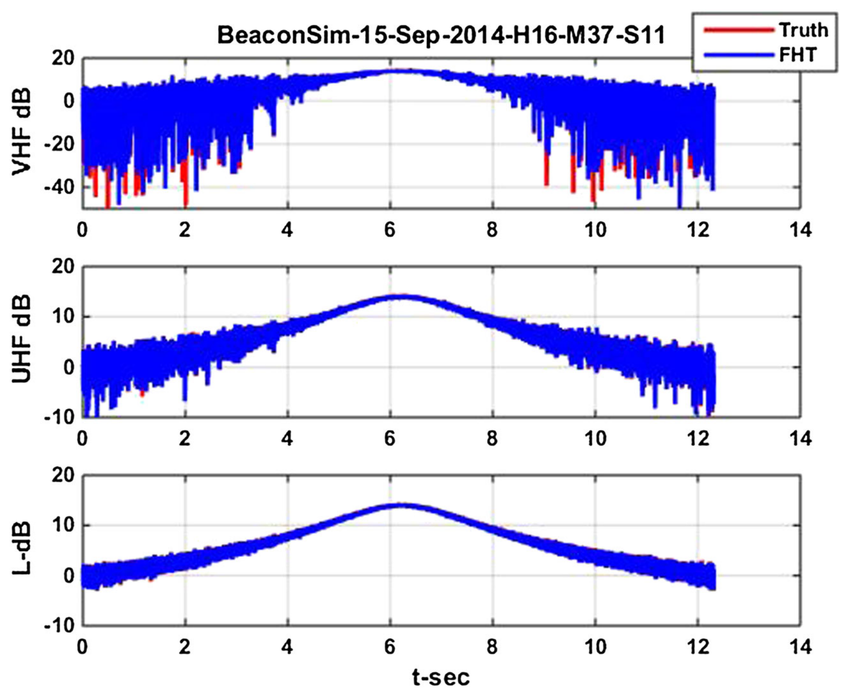

Figure 13. Intensity scintillation derived by dynamic demodulation with denoised FHT Doppler estimate (blue) overlaid on the intensity truth (red).

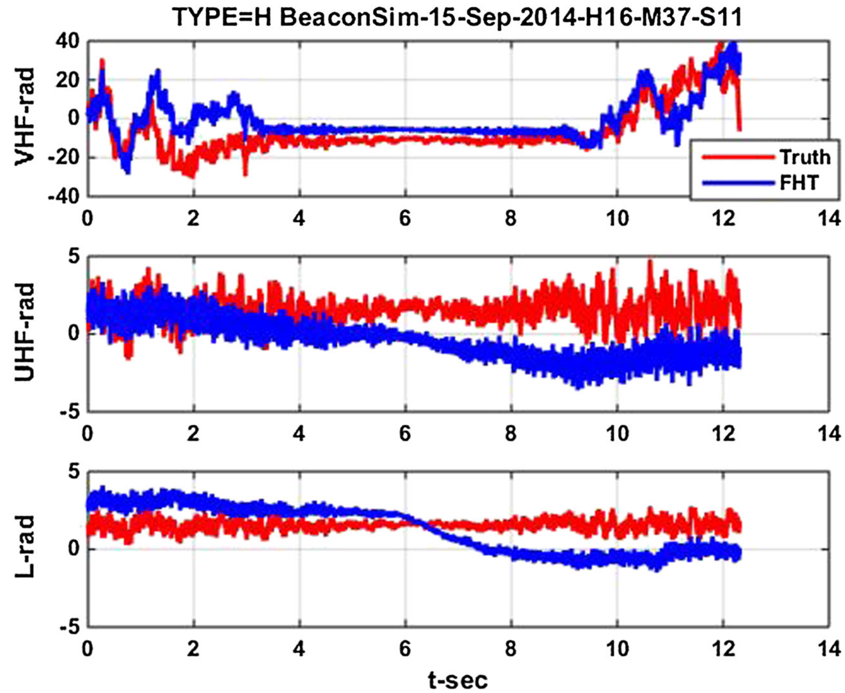

Figure 14. Phase scintillation derived by dynamic demodulation with denoised FHT Doppler estimate (blue) overlaid on the phase truth (red).

TEC estimates can be used to correct range estimates. Figure 11 shows the errors for corrected range estimates derived from

$$\hat{r}_k = \varphi_k c/\left(2\pi f_C\right) + K\widehat{\widehat{N}}_k c/\left(2\pi f_C^2\right), \tag{33}$$

with the average TEC and dual-frequency T realization phase estimates. The errors are essentially the same as shown in Figure 9. These expected results verify the FHT tracker operation in the absence of scintillation.

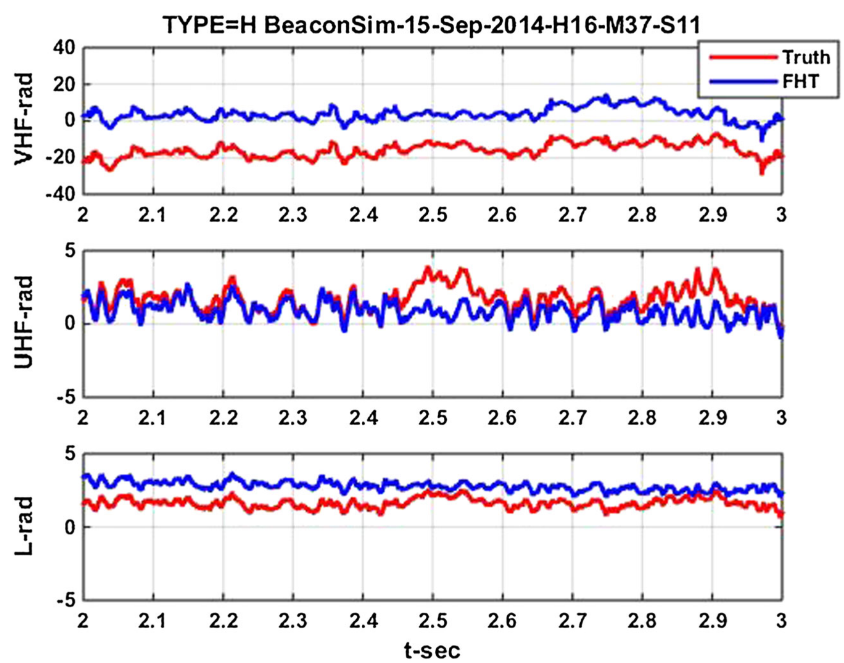

Figure 15. Zoomed in 1 s segment of phase scintillation shown in Figure 14.

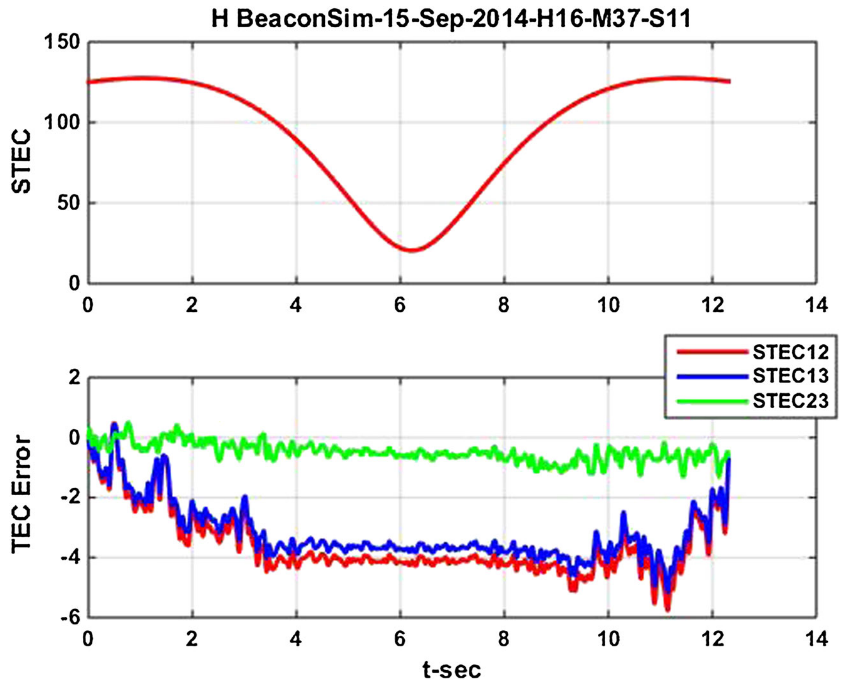

Figure 16. TEC estimates derived from H realization denoised Doppler.

The results also illustrate SNR-limited performance bounds. The results were obtained at SNR levels that can be achieved with good engineering design.

3.2. Scintillation Diagnostics

Single-frequency measurements must contend with geometric Doppler, TEC, and scintillation, which occupy overlapping time scale ranges. Results presented in section 3.1 showed that the geometric Doppler and TEC contributions are fully captured at the 24 Hz rate. The strategy here is to use the denoised Doppler to dynamically demodulate the complex signal. To the extent that the denoised Doppler retains *only* the geometric and TEC components, the scintillation phase is recovered. Figure 12 summarizes the FHT VHF Doppler as derived from H realizations. Upon comparing Figures 12 and 8 with allowance for the near order-of-magnitude change of scale, it is clear that the denoised Doppler residual (blue) retains structure that lies in the transition from TEC to phase scintillation.

Because the dynamic demodulation operation does not affect signal intensity, we expect the scintillation intensity estimate to faithfully reproduce the truth. This is demonstrated in Figure 13, which shows VHF, UHF, and L band scintillation intensity estimates downsampled to 500 Hz (blue). The results are overlaid on the noise-limited intensity truth from (6). The suppression of the deepest fades, which are approaching the noise level, is attributed to SNR limitations.

Figure 14 shows the VHF, UHF, and L band phase scintillation estimates. The systematic departures are attributed to the residual structure in the denoised Doppler. Because there is no theory that addresses phase scintillation under strong scatter conditions, these should be of little concern. Figure 15 shows an expanded plot of a 1 s data segments. The small-scale structure is preserved. It is predominantly the high-frequency structure that can be exploited for interpreting phase scintillation.

Figure 16 shows the result of using phase from the denoised Doppler estimates to calculate TEC. Because TEC would be calibrated independently, the offsets from the zero starting point are not significant. The results show that estimates with frequency pairs that use the saturated VHF scintillation can exceed 4 TEC units. For most TEC applications, this is an acceptable error. The result supports the generally accepted conclusion that as long as the SNR exceeds the lock threshold, TEC estimates are viable with the stated error bounds.

4. Summary and Conclusions

This paper demonstrates a digital processing algorithm for digitally recorded baseband beacon satellite signals. As currently configured, the algorithm first estimates the slowly varying Doppler component of the signal by applying the FHT estimator. Coherent processing gains of more that 30 dB support the fine frequency estimation. A 24 Hz report interval captures the geometric Doppler and TEC contributions to the signal phase. A second operation uses the denoised FHT Doppler estimates to dynamically demodulate the full-bandwidth signal. The demodulated signal, which carries the frequency content above 24 Hz, is downsampled and filtered to a bandwidth that captures the complex scintillation. Because the demodulation operation only affects the signal phase, the intensity scintillation preserves the full frequency range.

At the SNR levels used for the simulations, both TEC and scintillation components are recovered with high fidelity, as verified by direct comparisons to the input truth. The real-world challenge of identifying the phase-structure components that can be interpreted as path-integrated phase and the large-scale structure generated by diffraction remains, but FHT processing is well suited for generating appropriate data for study.

The FHT tracking operation uses a time-consuming search to generate refined Doppler estimates. Processing the 50 kHz data segments with unoptimized code required approximately 20 min of processing on a high-end PC per frequency. The orbital period for a typical low-orbiting CERTO beacon is 100 min. Thus, it is feasible to process recorded data between passes.

A minimum peak-hypothesis SNR (typically 15 dB) is required. Below this threshold, the FHT reports the complex signal at the nominal frequency for reacquisition, which is usually noise. Phase is reset to zero. In real-world applications, below threshold data are flagged as unusable. In effect, the FHT tracker makes a distinction between loss of signal and rapid phase variations as the signal approaches the front-end noise level. Although the excised reports have no cycle slips, the starting phase is reset to zero. In this situation, the unknown starting phase of reinitiated data segments often can be partially recovered by adjusting the segment offsets for extrapolated continuity.

Appendix A: Circular Orbit

$$\dot{\omega} = 2\pi/T_p, \tag{A1}$$

where T_p is the orbital period. The orbital velocity at height H is

$$v_p = \dot{\omega}\left(R_E + H\right), \tag{A2}$$

where R_E is the Earth radius. The following formulae, respectively, define the satellite (at height H_s) and penetration point (at height H_p) positions in Earth-centered coordinates:

$$X = \left(R_E + H_s\right)\sin(\dot{\omega}) \tag{A3}$$

$$Z = \left(R_E + H_s\right)\cos(\dot{\omega}) \tag{A4}$$

$$X_P = \left(R_E + H_P\right)\sin(\dot{\omega}t) \tag{A5}$$

$$Z_P = \left(R_E + H_P\right)\cos(\dot{\omega}t). \tag{A6}$$

For a receiver at $X = 0$ and $Z = R_E$, the elevation angle to the satellite is

$$\varphi = \arctan\left(\left(Z - R_E\right)/X\right) \tag{A7}$$

$$= \arctan\left(\frac{\left(1 + H_s/R_E\right)\cos(\dot{\omega}t) - 1}{\left(1 + H_s/R_E\right)\sin(\omega t +)}\right). \tag{A8}$$

The satellite is visible for positive elevation angles

$$\left|t_{\text{vis}}\right| > \arccos\left(1/\left(1 + H/R_E\right)\right)/\dot{\omega}. \tag{A9}$$

The range and range rate are readily computed as

$$r/R_E = \sqrt{\left(1 + H/R_E\right)^2 - 2\left(1 + H/R_E\right)\cos(\dot{\omega}t) + 1}, \tag{A10}$$

and

$$\dot{r}/R_E = \frac{\left(1 + H/R_E\right)\sin(\dot{\omega}t)\dot{\omega}}{\sqrt{\left(1 + H/R_E\right)^2 - 2\left(1 + H/R_E\right)\cos(\dot{\omega}t) + 1}}. \tag{A11}$$

The great circle angle to the satellite is

$$\theta_e = \cdot\omega t. \tag{A12}$$

The angle to the penetration point, its cosine, and secant are

$$\theta_p = \arctan\left(\frac{\sin\theta_e}{1 + H_p/R_E - \cos\theta_e}\right) \tag{A13}$$

$$\cos\theta_p = \frac{1 + H_p/R_E - \cos\theta_e}{\sqrt{\left(1 + H_p/R_E\right)^2 - 2\left(1 + H_p/R_E\right)\cos\theta_e + 1}} \tag{A14}$$

$$\sec\theta_p = \frac{\sqrt{\left(1 + H_p/R_E\right)^2 - 2\left(1 + H_p/R_E\right)\cos\theta_e + 1}}{\left(1 + H_p/R_E\right) - \cos\theta_e}. \tag{A15}$$

The TEC Doppler shift requires the derivatives

$$\frac{\mathrm{d}}{\mathrm{d}t}\sec\theta_p = \sec\theta_p \tan\theta_p \dot{\theta}_p \tag{A16}$$

and

$$\dot{\theta}_p = \frac{1 - \cos\theta_e\left(1 + H_p/R_E\right)}{\left(1 + H_p/R_E\right)^2 - 2\cos\theta_e\left(1 + H_p/R_E\right) + 1}\dot{\omega}. \tag{A17}$$

Acknowledgments
This work was sponsored by the Air Force contract FA87-18-09-C-0041. All of the results shown in the paper are simulations. No actual data were used.

References

Basu, S., S. Basu, J. P. McClure, W. B. Hanson, and H. E. Whitney (1983), High resolution topside in situ data of electron densities and VHF/GHz scintillations in the equatorial region, *J. Geophys. Res.*, *88*(A1), 403–415, doi:10.1029/JA088iA01p00403.

Bernhardt, P. A., and C. L. Siefring (2008), New satellite-based systems for ionospheric tomography and scintillation region imaging, *Radio Sci.*, *41*, RS5S23, doi:10.1029/2005RS003360.

Boashash, B. (1992a), Estimating and interpreting the instantaneous frequency of a signal-part 1: Fundamentals, *Proc. IEEE*, *80*(4), 32–45.

Boashash, B. (1992b), Estimating and interpreting the instantaneous frequency of a signal-2: Algorithms and applications, *Proc. IEEE*, *80*(4), 540–568.

Carrano, C., C. E. Valladares, and K. M. Groves (2012), Latitudinal and local time variation of ionospheric turbulence parameters during the conjugate point equatorial experiment in Brazil, *Int. J. Geophys.*, *2012*, 103,936, doi:10.1155/2012/103963.

Fremouw, E. J., R. L. Leadabrand, R. C. Livingston, M. D. Cousins, C. L. Rino, B. C. Fair, and R. A. Long (1978), Early results from the DNA wideband satellite experiment—Complex-signal scintillation, *Radio Sci.*, *13*(1), 167–187.

Lee, T. H., and A. Hajimiri (2000), Oscillator phase noise: A tutorial, *IEEE J. Solid-State Circuits*, *35*(3), 326–336.

Mallat, S. (2005), *A Wavelet Tour of Signal Processing The Sparse Way*, Acad. Press, Boston, Mass.

Yamamoto, M. (2008), Digital beacon receiver for ionospheric TEC measurement developed with GNU radio, *Earth Planets Space Lett.*, *60*, 21–24.

Rino, C. L. (2011), *The Theory of Scintillation With Applications in Remote Sensing*, New York.

Swenson, G. W. (1994), Reminiscence: At the dawn of the space age, *J. Geophys. Res.*, *88*(A1), 403–415.

Tsui, J. B. -Y. (2005), *Fundamentals of Global Positioning System Receivers a Software Approach*, 1995, John Wiley, New York.